crystals

MDPI

Article

Novel $Y_2(SO_4)_3$:Eu^{3+} Phosphors with Anti-Thermal Quenching of Luminescence Due to Giant Negative Thermal Expansion

Andrey P. Shablinskii [1], Olga Yu. Shorets [1], Alexey V. Povotskiy [2], Rimma S. Bubnova [1,*], Maria G. Krzhizhanovskaya [3], Svetlana Yu. Janson [3], Valeri L. Ugolkov [1] and Stanislav K. Filatov [3]

[1] Institute of Silicate Chemistry of the Russian Academy of Sciences (ISC RAS), Makarova Emb. 2, St. Petersburg 199034, Russia; shablinskii.andrey@mail.ru (A.P.S.); olga_frooze@rambler.ru (O.Y.S.); ugolkov.52@mail.ru (V.L.U.)
[2] Institute of Chemistry, St. Petersburg State University, Universitetskaya Emb. 7/9, St. Petersburg 199034, Russia; alexey.povolotskiy@spbu.ru
[3] Institute of Earth Sciences, St. Petersburg State University, Universitetskaya Emb. 7/9, St. Petersburg 199034, Russia; krzhizhanovskaya@mail.ru (M.G.K.); jansn.sv@gmail.com (S.Y.J.); filatov.stanislav@gmail.com (S.K.F.)
* Correspondence: rimma_bubnova@mail.ru

Abstract: One of the most critical problems for phosphors used in light-emitting diodes (LEDs) is the thermal quenching of luminescence. Herein, novel $(Y_{1-x}Eu_x)_2(SO_4)_3$ (x = 0, 0.17, 0.33, 0.5, 0.66) phosphors with anti-thermal quenching of luminescence due to giant negative thermal expansion were obtained by crystallization from aqueous solutions. The $Y_2(SO_4)_3$ crystal structure is described as a framework, which consists of corner-sharing SO_4 tetrahedra and YO_6 octahedra. Thermal expansion of x = 0, 0.17, 0.5 solid solutions was investigated by high-temperature powder X-ray diffraction. The crystal structure of the x = 0.5 solid solution was refined by the Rietveld refinement using X-ray powder diffraction data at 400 and 500 °C to R_B = 1.7 and 1.9%, respectively. The rotation of the SO_4 tetrahedra results in giant negative volumetric thermal expansion: the structure contracts in all directions ($\alpha_a = -7(3)$, $\alpha_b = -15(3)$, $\alpha_c = -22(2)$, $\alpha_V = -44(2) \cdot 10^{-6}$ °C^{-1} at 500 °C for $YEu(SO_4)_3$). The photoluminescence intensity is enhanced 1.8 times with the temperature increasing up to 500 °C. The anti-thermal quenching of Eu^{3+} luminescence can be described in terms of thermal-enhanced energy transfer between Eu^{3+} ions due to the negative thermal expansion of the $Y_2(SO_4)_3$ matrix in all non-equivalent directions.

Keywords: anti-thermal quenching of luminescence; negative thermal expansion; phosphors; sulfates; crystal structure

check for updates

Citation: Shablinskii, A.P.; Shorets, O.Y.; Povotskiy, A.V.; Bubnova, R.S.; Krzhizhanovskaya, M.G.; Janson, S.Y.; Ugolkov, V.L.; Filatov, S.K. Novel $Y_2(SO_4)_3$:Eu^{3+} Phosphors with Anti-Thermal Quenching of Luminescence Due to Giant Negative Thermal Expansion. *Crystals* **2024**, *14*, 1074. https://doi.org/10.3390/cryst14121074

Received: 7 November 2024
Revised: 4 December 2024
Accepted: 9 December 2024
Published: 13 December 2024

Copyright: © 2024 by the authors. Licensee MDPI, Basel, Switzerland. This article is an open access article distributed under the terms and conditions of the Creative Commons Attribution (CC BY) license (https://creativecommons.org/licenses/by/4.0/).

1. Introduction

Recently, phosphor-converted white light-emitting diodes (pc-WLEDs) have garnered significant interest due to their environmental friendliness, reliability, and high luminous efficiency [1–6]. Phosphors are crucial in pc-WLEDs, as they influence luminous efficacy, color temperature, and lifetime. The luminescent characteristics of rare earth element-activated materials are highly dependent on the matrix [7,8]. Therefore, the selection of a suitable matrix is an important factor in improving luminescence and color purity. Well-proven matrices for luminescent materials include oxides [9,10], silicates [11–13], aluminates [14–16], phosphates [17,18], and borates [19–21]. In phosphors, the color of the emitted radiation depends not only on the activator ion, but also on the symmetry and environment of the active luminescence center in the crystal structure. In addition, knowledge of the crystal structure allows one to calculate the distance between the activated centers in the crystal structure, and thus predict the concentration or thermal quenching of luminescence [22]. One of the most critical problems for phosphors is thermal stability, as heat is generated during LED operation [23–26].

Thermal quenching of photoluminescence is one of the serious limiting factors for high-power white-emitting LEDs with increasing temperature, which leads to radiation losses due to an increase in the number of non-radiative transitions [27]. Consequently, the development of new phosphors that offer both high luminance and thermal stability remains a significant challenge and has attracted considerable attention [1,26–29]. In recent years, materials with thermal zero- or anti-thermal quenching of luminescence have been studied due to the use of compounds with zero or negative thermal expansion. As far as we know, the first example of the phosphor with anti-thermal quenching of luminescence due to negative thermal expansion is $Yb_2W_3O_{12}$:Y and $Yb_2W_3O_{12}$:Er [30]. Negative or zero thermal expansion does not allow energy to dissipate during the transition of photoluminescence centers from the excited state to the ground state due to thermal vibrations of the lattice, according to the works [6,31,32]. One of the possible areas of application for such photoluminescent materials is high-temperature sensors.

A well-known family of materials of the $Al_2(WO_4)_3$ structure type includes, in addition to tungstates, phosphates, molybdates, and sulfates [33–36]. Their crystal structures consist of structural blocks composed of an octahedron linked at the vertices with six tetrahedra. The framework consisting of these blocks is formed by relatively weak bonds and has large cavities. With an increase in temperature, due to the rotation of the tetrahedra, hinge deformation occurs; the blocks are displaced into the cavities of the framework, which leads to a strong negative volumetric thermal expansion $\alpha_V = -33 \times 10^{-6}\ ^\circ C^{-1}$ [34]. This negative thermal expansion occurs in the $Al_2(WO_4)_3$ family over the entire temperature range below 1170 °C [35].

Thus, here novel anti-thermal quenching $(Y_{1-x}Eu_x)_2(SO_4)_3{*}8H_2O$ (x = 0, 0.17, 0.33, 0.5, 0.66) phosphors of $Al_2(WO_4)_3$ structure type with giant negative thermal expansion were prepared by crystallization from aqueous solutions. Thermal expansion and photoluminescence of all samples were investigated and the crystal structures were refined. The mechanisms of negative thermal expansion and anti-thermal quenching of luminescence are described.

2. Materials and Methods

2.1. Synthesis

Phosphors were crystallized from aqueous solutions. Firstly, two supersaturated solutions of $Y_2(SO_4)_3$ (Vekton, 99.99% purity) and $Eu_2(SO_4)_3$ (Vekton, 99.99% purity) were prepared. Then, they were mixed in the appropriate stoichiometric ratios, and these solutions were poured into Petri dishes and waited for the crystals to precipitate from the solution. In this way, 5 precursor samples were obtained $(Y_{1-x}Eu_x)_2(SO_4)_3{*}8H_2O$: x = 0, 0.17, 0.33, 0.5, 0.66. Finally, all samples were calcined at 400 °C for 3 h. Figure 1 shows a sample with a 1:1 stoichiometry.

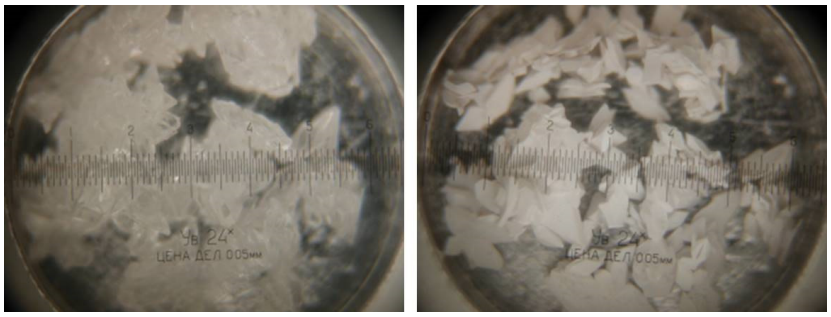


Figure 1. Crystals of $(Y_{0.5}Eu_{0.5})_2(SO_4)_3{*}8H_2O$ (**left**) and $(Y_{0.5}Eu_{0.5})_2(SO_4)_3$ (**right**).

2.2. Powder X-Ray Diffraction

Powder diffraction data for $(Y_{1-x}Eu_x)_2(SO_4)_3{*}8H_2O$ (x = 0, 0.17, 0.33, 0.5, 0.66) samples were collected using a Rigaku MiniFlex II diffractometer (CuKα, 2θ = 3–60°, step 0.02).

The phase composition was determined using PDXL-integrated X-ray powder diffraction software and the PDF-2 2020 (ICDD) database.

Powder diffraction data for the Rietveld refinement of $(Y_{0.5}Eu_{0.5})_2(SO_4)_3$ were collected using a Rigaku Ultima IV diffractometer (CuKα_{1+2}, 40 kV and 35 mA, Bragg-Brentano geometry, PSD DTEX/ULTRA detector, SHT–1500 high-temperature camera, 2θ = 8–100°, step 0.02°, exposure at point 5 s). Experimental data processed by the Rietveld refinement, such as the refinement of zero shift, background approximation, peak shape parameters, unit cell parameters, atomic coordinates, and isotropic displacement parameters, were performed using RTT software [37] (Figures S1 and S2). A starting model for the refinement was $Y_2(SO_4)_3$ (*Pbcn*; ICSD № 411220). Pseudo-Voight functions were used for fitting the reflection profiles. The background was described by a Chebyshev polynomial function (20rd order). Crystallographic data and refinement parameters are given in Table 1; atomic coordinates, isotropic displacement parameters, and selected bond lengths are given in Tables 2 and S1. Further details of the crystal structure investigations can be obtained from the Cambridge Structural Database by quoting the depository numbers CSD 2401196 and 2401199.

Table 1. Structure refinement details and crystallographic data for $YEu(SO_4)_3$.

Formula	**$YEu(SO_4)_3$**	
Temperature (°C)	400	500
Crystal system, Space group, Z	Orthorhombic, *Pbcn*, 4	
a (Å)	12.8354(2)	12.8298(1)
b (Å)	9.1616(1)	9.1528(1)
c (Å)	9.25824(1)	9.2534(1)
Volume (Å^3)	1088.70(4)	1086.62(4)
Radiation type	Cu $K\alpha_{1+2}$	
2θ range (deg.)	8–100	
Number of points	4600	4600
R_p	0.0162	0.0195
R_{wp}	0.0251	0.0283
R_{exp}	0.0081	0.0082
R_B	0.0170	0.0194
GOF	3.09	3.48

Table 2. Selected bond lengths (Å) for $YEu(SO_4)_3$ at different temperatures.

400 °C		**500 °C**	
Bond	**Distance, Å**	**Bond**	**Distance, Å**
(Y,Eu1)–O1	2.168(4)	(Y,Eu1)–O1	2.172(6)
(Y,Eu1)–O6	2.235(4)	(Y,Eu1)–O6	2.193(6)
(Y,Eu1)–O2	2.238(4)	(Y,Eu1)–O2	2.228(7)
(Y,Eu1)–O3	2.368(4)	(Y,Eu1)–O3	2.421(6)
(Y,Eu1)–O4	2.395(4)	(Y,Eu1)–O4	2.409(7)
(Y,Eu1)–O5	2.411(5)	(Y,Eu1)–O5	2.463(8)
<(Y,Eu1)–O>$_6$	2.30	<(Y,Eu1)–O>$_6$	2.31
S1–O5	1.365(5)	S1–O5	1.394(9)
S1–O1	1.408(4)	S1–O1	1.397(7)
S1–O3	1.433(6)	S1–O3	1.435(9)
S1–O6	1.469(5)	S1–O6	1.497(7)
<S1–O>$_4$	1.42	<S1–O>$_4$	1.43
S2–O4 × 2	1.393(5) × 2	S2–O4 × 2	1.391(8) × 2
S2–O2 × 2	1.444(4) × 2	S2–O2 × 2	1.503(7) × 2
<S2–O>$_4$	1.42	<S2–O>$_4$	1.45

2.3. Energy-Dispersive X-Ray Spectroscopy

The chemical composition was studied using a system with focused electron and ion probes QUANTA 200 3D (FIA, The Netherlands) with an energy-dispersive spectroscopy analytical complex Pegasus 4000 (EDAX, Pleasanton, CA, USA). The analytical spectra were obtained from a smooth crystal surface at an operating voltage of 20 kV, with a beam size of 1 μm. The samples were coated with carbon. Analytical results are given in Table S2.

2.4. Differential Scanning Calorimetry

The differential scanning calorimetry (DSC) and thermogravimetry (TG) studies of $Y_2(SO_4)_3$*$8H_2O$ were performed on NETZSCH STA 429 (NETZSCH, Hanau, Germany) with the use of a standard sample holder for measuring the (DSC) and (TG) curves. The sample in the form of tablets was placed in a platinum crucible and heated up to 1250 °C in air at a rate of 20 °C/min. The sample weight was 22.7 mg. The temperatures of the thermal effects were estimated as onset temperatures. A change in the sample weight was controlled from the TG curves.

2.5. High-Temperature Powder X-Ray Diffraction

Thermal expansion for three samples ($(Y_{1-x}Eu_x)_2(SO_4)_3$*$8H_2O$: x = 0, 0.17, 0.5) was studied by high-temperature X-ray powder diffraction using a Rigaku Ultima IV diffractometer ($CuK\alpha_{1+2}$, 40 kV and 35 mA, Bragg-Brentano geometry, PSD DTEX/ULTRA detector, SHT–1500 high-temperature camera, 2Θ = 5–70°, step width: 0.02°, total counting time of about 2 s per step). The average heating rate was about 0.4 °C/min. Unit cell parameters were refined at different temperatures by the Rietveld method using RietveldToTensor software [37]. The thermal behavior was studied using in situ high-temperature powder X-ray diffraction in the range of 25–600 °C.

Coefficients of approximation of temperature dependences of unit cell parameters, eigenvalues, and figures of thermal expansion tensor were calculated using RietveldToTensor software [37]. Using the approximation coefficients of temperature dependences of unit cell parameters, the tensor components were in the Cartesian crystallophysical coordinate system.

Based on the calculated eigenvalues of the tensor, the surface of the second-rank symmetric tensor or, in other words, the figure of thermal expansion coefficients can be plotted as a 3D model. Each radius vector of this figure represents the value of the thermal expansion coefficient in a certain direction.

2.6. Photoluminescence

Photoluminescence (PL) spectra were measured with a T64000 spectrometer (Horiba Jobin Yvon, Oberursel, Germany) equipped with a confocal microscope. Excitation of fluorescence was realized with the use of 375 nm diode laser CUBE (Coherent). The quantum yield was determined by comparison with the known quantum yield of a polycrystalline sample $BaBi_{1.6}Eu_{0.4}B_4O_{10}$ [38]. The temperature dependence of luminescence was determined using a TS1500 stage (Linkam, Redhill, UK). Before the measurement, the x = 0.17 solid solution was heated to 600 °C and held for 1 h. Then, this solid solution was cooled to 150 °C and the luminescence spectra were measured with the temperature increasing in 25 °C increments. The heating rate was 20 °C per minute.

3. Results and Discussion

3.1. Morphology and Chemical Composition

To evaluate the morphology of these phosphors, optical microscopy images before and after heating at room temperature are shown in Figure 1. The shapes of the powders before heating are prismatic crystals with lengths of 1.5 mm and a width of 0.5 mm. The crystals after heating have practically the same dimensions, but are more flattened, which is manifested in the texturing of the sample along the direction (010), revealed

during refinement by the Rietveld method. Such a texture is characteristic of compounds crystallizing in this structure type [39].

The empirical formulae calculated on the basis of two cations per formula unit for $x = 0.17$ and 0.50 are $Y_{1.72}Eu_{0.28}(SO_4)_3{*}8H_2O$ and $Y_{0.96}Eu_{1.04}(SO_4)_3{*}8H_2O$, which are in good agreement with the powder X-ray diffraction data. The content of crystallization water was not measured.

3.2. Powder X-Ray Diffraction of the $(Y_{1-x}Eu_x)_2(SO_4)_3{*}8H_2O$: x = 0, 0.17, 0.33, 0.5, 0.66 Precursors

X-ray phase analysis at room temperature revealed that $(Y_{1-x}Eu_x)_2(SO_4)_3{*}8H_2O$ ($x = 0$, 0.17, 0.33, 0.5, 0.66) precursors are homogeneous (Figure 2). Since the objects of the present study are the $(Y_{1-x}Eu_x)_2(SO_4)_3$ phosphors, we performed an X-ray phase analysis in the high-temperature region (400 °C). The results showed that these phosphors are also homogeneous (Figure 3).

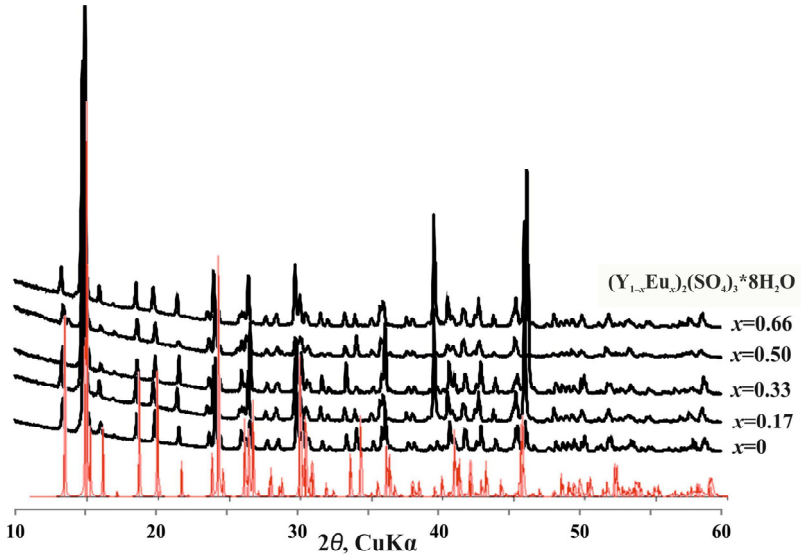


Figure 2. Powder X-ray diffraction patterns of the $(Y_{1-x}Eu_x)_2(SO_4)_3{*}8H_2O$ precursors. Red lines mark the calculated powder XRD pattern of $Y_2(SO_4)_3{*}8H_2O$ [40].

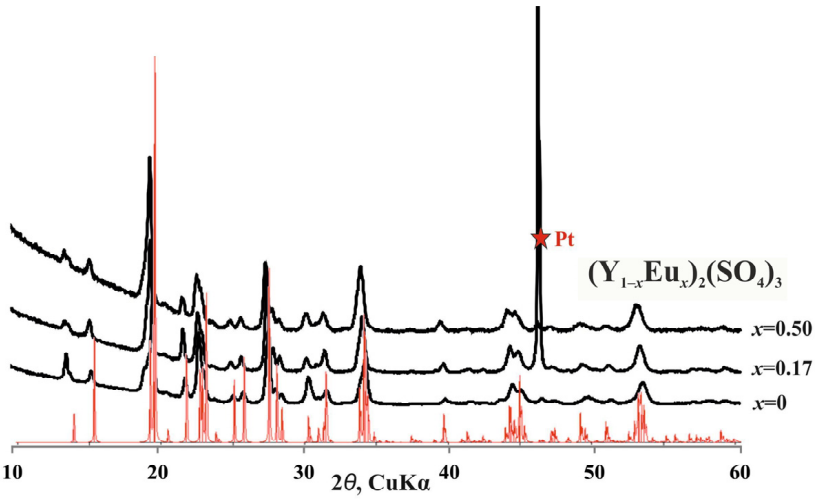


Figure 3. Some powder X-ray diffraction patterns of the $(Y_{1-x}Eu_x)_2(SO_4)_3$ solid solutions at 400 °C. Red lines mark the calculated powder XRD pattern of $Y_2(SO_4)_3$ [41].

3.3. Thermal Transformations of $(Y_{1-x}Eu_x)_2(SO_4)_3{*}8H_2O$

Thermal transformations (dehydration and decomposition with the formation of other crystalline phases and the release of volatile components) of $(Y_{1-x}Eu_x)_2(SO_4)_3{*}8H_2O$ solid solutions were investigated by DSC, TG, HTXRD, and annealing methods.

DSC and TG study of $Y_2(SO_4)_3{*}8H_2O$ aqueous sulfate. For example, the heating DSC and TG curves for $Y_2(SO_4)_3{*}8H_2O$ are presented in Figure 4. There are four thermal effects in the DSC curve and three mass losses in the TG one. The first endo-effect starts at about 90 °C; its maximum is split slightly at 182 and 187 °C. This most intensive peak corresponding to the dehydration process is accompanied by mass losses of 23.97% in accord with the reaction: $Y_2(SO_4)_3{*}8H_2O = Y_2(SO_4)_3 + 8H_2O\uparrow$. These data are in good agreement with the calculation of the loss of eight water molecules, which is 23.60 wt%. The next very weak exo-effect in the temperature range of 267–325 °C can be attributed to the formation (crystallization) of the anhydrous $Y_2(SO_4)_3$ phase by self-dispersion of powder particles due to the volatilization of water molecules. With further heating, a two-stage thermal decomposition of the anhydrous sulfate occurs with the release of volatile components. The following two endo-effects observed in the DSC curve are broadened: their onsets are at 787 and 1033 °C, and the maxima are at 984 and 1132 °C, respectively. They are accompanied by mass losses of 27.47% and 13.77%. First, during the volatilization of SO_3, oxysulfate $Y_2O_2(SO_4)$ is formed according to the reaction: $Y_2(SO_4)_3 = Y_2O_2(SO_4) + 2SO_3\uparrow$. The $Y_2O_2(SO_4)$ oxysulfate was obtained by annealing $Y_2(SO_4)_3$ at 1000 °C for 5 h. Its powder diffraction pattern is similar to those of $Eu_2O_2(SO_4)$ [42]. At the second stage of decomposition, either $SO_2 + O_2$ or SO_3 volatilizes as a gas phase according to one of the reactions: $Y_2O_2(SO_4) = Y_2O_3 + SO_2\uparrow + 0.5\ O_2\uparrow$ or $Y_2O_2(SO_4) = Y_2O_3 + SO_3\uparrow$. As a result of decomposition, in both cases, Y_2O_3 yttrium oxide remains in a solid phase. This interpretation of the peaks at temperatures of 787 and 1033 °C is in good agreement with the calculation of mass loss, according to which 26.25 and 13.12 wt.% are lost during decomposition, respectively.

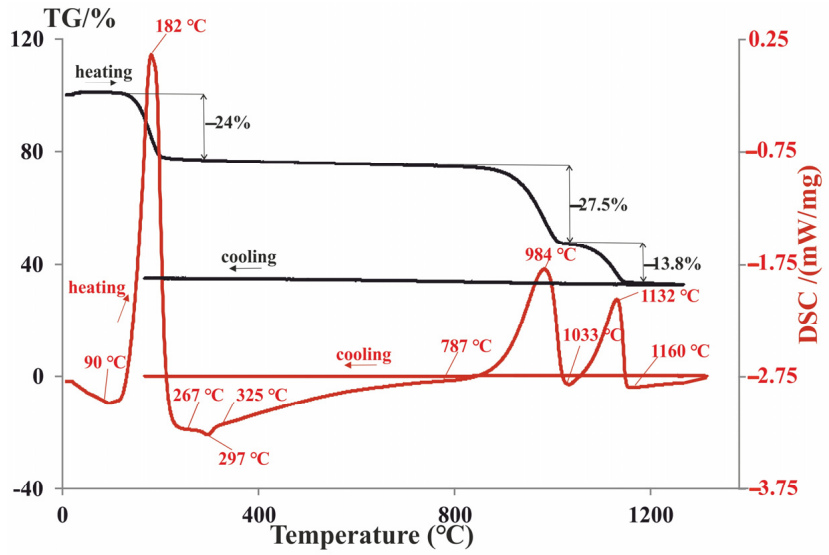


Figure 4. DSC and TG data for $Y_2(SO_4)_3{*}8H_2O$.

HTXRD study of $(Y_{1-x}Eu_x)_2(SO_4)_3{*}8H_2O$ solid solutions. Three homogeneous samples $(Y_{1-x}Eu_x)_2(SO_4)_3{*}8H_2O$ with $x = 0$, 0.17, 0.5 were studied by HTXRD. Firstly, these samples were heated up to 600 °C. Then, the solid solutions were cooled and reheated to 600 °C. Figure 5 shows phase transformations of $(Y_{0.83}Eu_{0.17})_2(SO_4)_3$, as an example. Solid solutions $(Y_{1-x}Eu_x)_2(SO_4)_3{*}8H_2O$ remain stable up to about 120 °C with increasing temperature. In all three samples, we observed a similar pattern.

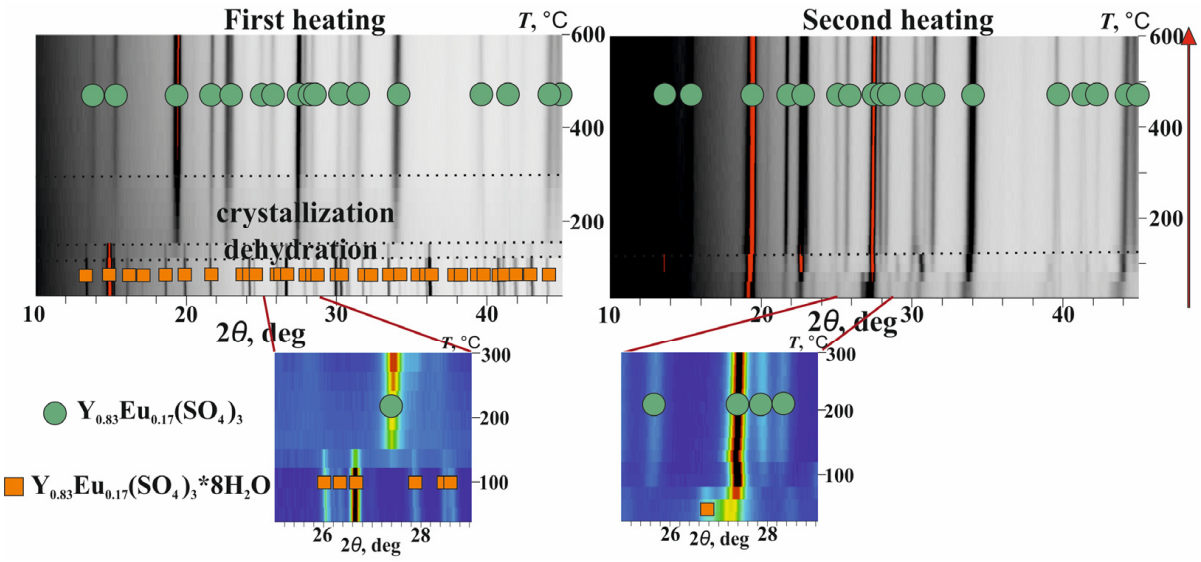


Figure 5. Thermal phase transformations of $(Y_{0.83}Eu_{0.17})_2(SO_4)_3$.

During the first heating of $(Y_{1-x}Eu_x)_2(SO_4)_3$*$8H_2O$ from room temperature to about 120 °C, no sharp changes in the HTXRD pattern were observed. Within the region of 120–160 °C, peaks of this phase decrease and weak peaks of $(Y_{1-x}Eu_x)_2(SO_4)_3$ sulfates appear; hence, there exists a two-phased region. Above 160 up to 300 °C, the $(Y_{1-x}Eu_x)_2(SO_4)_3$ solid solutions are formed, the peaks position and width decrease, peaks intensities increase (left insert in Figure 5). Above 300 °C, we observed a homogeneous $(Y_{1-x}Eu_x)_2(SO_4)_3$ solid solutions. After cooling, the sulfates absorb an insignificant amount of water again (right insert in Figure 5). During the second heating up to 80 °C, the indistinct peaks of $(Y_{1-x}Eu_x)_2(SO_4)_3$*$8H_2O$ are preserved as well. The dehydration and formation of homogeneous $(Y_{1-x}Eu_x)_2(SO_4)_3$ sulfates are observed in the temperature range of 80–120 °C. Above 120 °C and up to 600 °C, only peaks of $(Y_{1-x}Eu_x)_2(SO_4)_3$ solid solutions are observed (Figure 5).

3.4. Thermal Expansion of $(Y_{1-x}Eu_x)_2(SO_4)_3$ Solid Solutions

Temperature dependencies of unit cell parameters and volume of $(Y_{1-x}Eu_x)_2(SO_4)_3$ solid solutions are shown in Figure 6. All unit cell parameters decrease with increasing temperature, which indicates contraction along all directions as well as volume, i.e., the so-called negative thermal expansion—an intriguing phenomenon—since most compounds expand with increasing temperature. Compounds with thermal expansion are very rare. The structure is most weakly contracted along the *a* axis, especially with contraction in all directions. The dependencies were approximated by a quadratic polynomial function. The equations and eigenvalues of the thermal expansion tensor calculated at several temperatures are given in Tables 3 and 4. It is noteworthy that the eigenvalues of negative thermal expansion in all directions increase with increasing temperature by one and a half times. According to [43–45], the volumetric thermal expansion of the samples $x = 0$, 0.17 and 0.50 belongs to giant negative thermal expansion ($\alpha_a = -7(3)$, $\alpha_b = -15(3)$, $\alpha_c = -22(2)$, $\alpha_V = -44(2) \cdot 10^{-6}$ °C^{-1} at 500 °C for $YEu(SO_4)_3$).

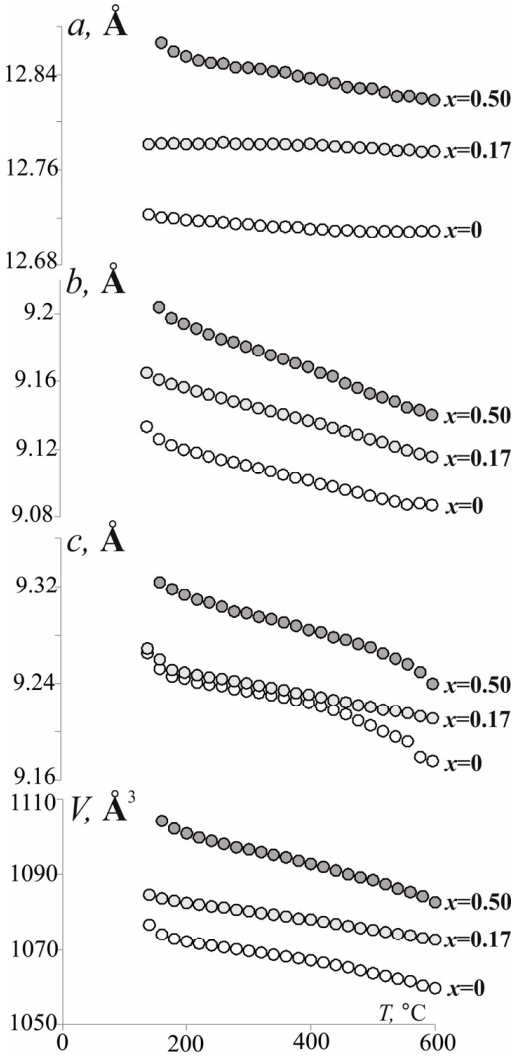


Figure 6. Temperature dependencies of unit cell parameters for $(Y_{1-x}Eu_x)_2(SO_4)_3$ solid solutions.

Table 3. Temperature dependencies of unit cell parameters for $(Y_{1-x}Eu_x)_2(SO_4)_3$ solid solutions as quadratic polynomials $a_0 + a_1 \times 10^{-3}t + a_2 \times 10^{-6}\ t$.

Parameter	a_0	a_1	a_2
	x = 0		
$a(t)$, Å	12.7496(74)	−0.185(39)	0.214(47)
$b(t)$, Å	9.1350(14)	−0.074(22)	−0.021(32)
$c(t)$, Å^2	9.2339(28)	0.095(14)	−0.303(17)
$V(t)$, Å^3	1075.71(54)	−14.7(28)	−18.0(34)
	x = 0.17		
$a(t)$, Å	12.7791(19)	0.025(45)	−0.054(11)
$b(t)$, Å	9.1734(65)	−0.082(27)	−0.025(44)
$c(t)$, Å^2	9.2684(12)	−0.093(51)	−0.003(22)
$V(t)$, Å^3	1086.44(26)	−18.2(13)	−8.1(7)
	x = 0.5		
$a(t)$, Å	12.8732(26)	−0.091(13)	−0.001(16)
$b(t)$, Å	9.2193(16)	−0.124(42)	−0.015(31)
$c(t)$, Å^2	9.3182(61)	0.000(32)	−0.206(31)
$V(t)$, Å^3	1105.98(69)	−23.2(35)	−25.1(43)

Table 4. Thermal expansion coefficients for $(Y_{1-x}Eu_x)_2(SO_4)_3$ solid solutions ($\times 10^{-6}$ °C $^{-1}$).

x	T, °C	α_a	α_b	α_c	α_V
0	300	−4(1)	−11(1)	−8(3)	−23(2)
	400	−2(3)	−10(2)	−17(3)	−29(2)
	500	−1(3)	−8(3)	−25(1)	−34(3)
0.17	300	−1(3)	−11(2)	−10(2)	−22(1)
	400	−2(1)	−11(1)	−11(1)	−23(1)
	500	−2(3)	−12(2)	−11(2)	−24(1)
0.5	300	−7(3)	−14(3)	−13(2)	−34(3)
	400	−7(1)	−15(1)	−17(1)	−39(3)
	500	−7(3)	−15(3)	−22(2)	−44(2)

3.5. Crystal Structure of $(Y_{1-x}Eu_x)_2(SO_4)_3$ Solid Solutions and Thermal Expansion

The $Y_2(SO_4)_3$ crystal structure was solved and refined in orthorhombic *Pbcm* space group in [41]. The $Y_2(SO_4)_3$ crystal structure crystallizes in the $Al_2(WO_4)_3$ structure type. There are one independent Y (8*d*) site, two S (8*d* and 4*c*) and six O (8*d*) sites in asymmetric unit. The S atoms are tetrahedrally coordinated by oxygen atoms with S–O bond lengths 1.455–1.459 and 1.448–1.454 Å, respectively. The Y site is surrounded by six oxygen atoms to form YO_6 octahedra with bond lengths are in 2.20–2.24 Å. The $Y_2(SO_4)_3$ crystal structure is isolated, since the SO_4 tetrahedra are not connected to each other. The structure is usually described as a heteropolyhedral framework. The heteropolyhedral framework consists of corner-sharing SO_4 tetrahedra and YO_6 octahedra. Each octahedron is linked to six tetrahedra, so that it forms a microblock (octahedral-tetrahedral cluster) derived by [46] (Figure 7).

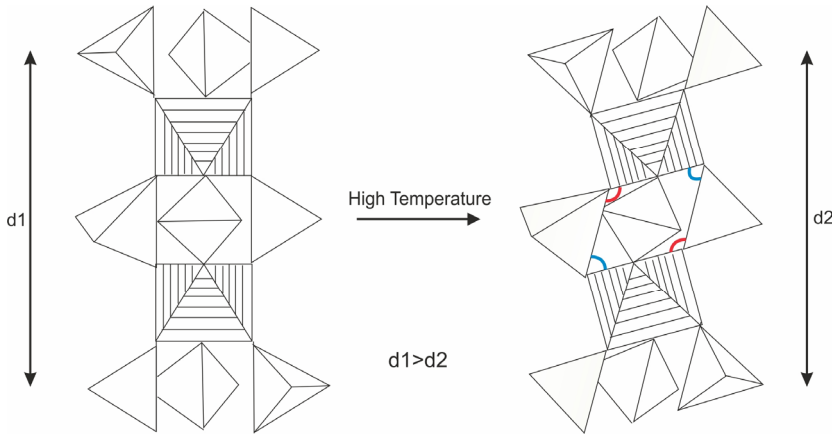


Figure 7. A schematic representation of microblock hinge (rocking polyhedra). increased and decreased *M*–O–*T* angles are depicted by red and blue lines.

In the $Y_2(SO_4)_3$ crystal structure, the negative thermal expansion in all those directions can be described in terms of rocking polyhedra [36]. A detailed description of the negative thermal expansion of this structure type is given in [33,34]. The authors described the rocking polyhedra of slabs (cf. Figure 8b) of the crystal structure. Now, we describe the thermal expansion of this crystal structure in terms of microblocks (octahedral-tetrahedral clusters).

In the $Y_2(SO_4)_3$ crystal structure, the corner-sharing with each other $Y(SO_4)_6$ microblocks can be considered as a hinge unit. Let us consider the mechanism of such a hinge unit. The O–O edges of rigid SO_4 tetrahedra and faces of YO_6 octahedra are the sides of the hinge, and the O atoms are the corners of the hinge. A schematic representation of the microblock hinge in terms of rocking polyhedra is shown in Figure 7. *M*–O–*T* angles increased (Figure 7, red lines) and decreased (Figure 7, blue lines). Therefore, the deformations of this hinge unit are sharply anisotropic, and it leads to a thermal contraction in the

direction along the *z* axis of the microblock and thermal expansion in the x and y directions of the microblock.

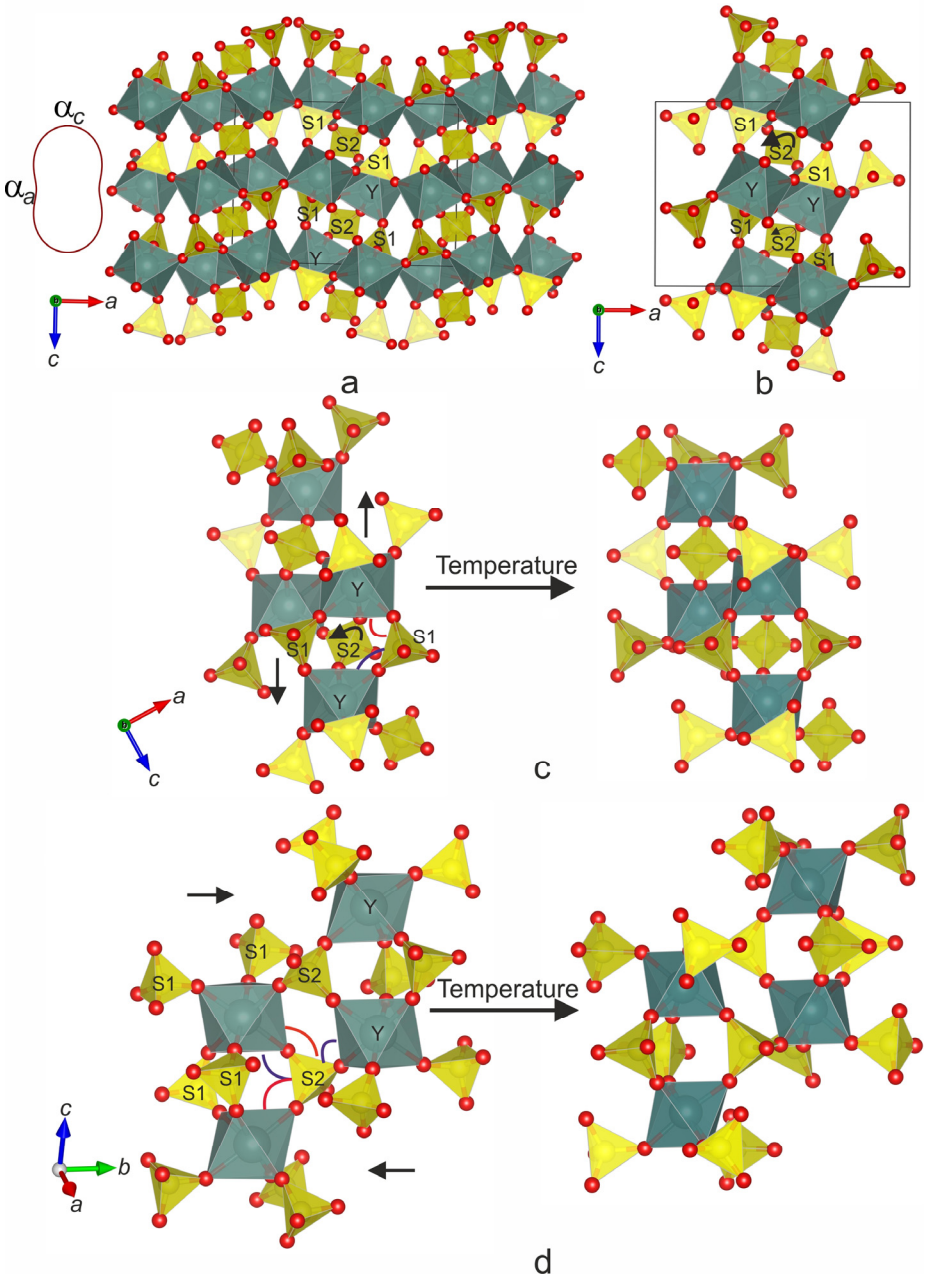


Figure 8. Interpretation of $Y_2(SO_4)_3$ thermal contraction based on the [34] data. (**a**) $Y_2(SO_4)_3$ crystal structure in *ac* projection in comparison with the figure of negative thermal expansion tensor (300 °C), (**b**) slab of $Y_2(SO_4)_3$, (**c**,**d**) changes in the branched chain with increasing temperature. Small arrows show the rotations of the polyhedra and the compression and extension of the branched chains.

But in this case, in the $Y_2(SO_4)_3$ crystal structure, the mechanism of thermal deformations is complicated by the fact that the microblocks in the crystal structure are already distorted, and the *M*–O–*T* angles (Y1–O5–S1 = 144.9(2)° and Y1–O4–S2 = 154.1(2)°) are far from 180°. In addition, the hinge mechanism described above explains the negative thermal expansion in only one direction well.

Based on the data and conclusions obtained in [34], it is known that of all the structural units, the tetrahedron $S2O_4$ changes its position most strongly with changes in temperature. As shown in Figure 8c, this tetrahedron rotates counterclockwise. This rotation of the $S2O_4$ tetrahedra and, to a lesser extent, the $S1O_4$ tetrahedra results in the microblocks being

stretched along their axis of extension and slightly compressed in perpendicular directions. These microblocks are not connected in a column, but through tetrahedrons, as shown in Figure 8c, becoming a branched chain of two microblocks. Therefore, the rotation of the tetrahedra, in addition to increasing the microblock, leads to the fact that the links of this chain (microblocks) shift relative to each other (Figure 8c,d). Hence, the entire chain becomes shorter. This thermal behavior of the microblock and the branched chains can explain the thermal contraction of the $Y_2(SO_4)_3$ crystal structure in all directions.

Refinement of the $YEu(SO_4)_3$ crystal structure at 400 and 500 °C shows complete correspondence to the $Al_2(WO_4)_3$ structure type. The (Y,Eu)1 site is octahedrally coordinated by oxygen atoms and (Y,Eu)1–O bonds are in the ranges of 2.168–2.411 (400 °C) and 2.172–2.463 Å, respectively. The S1 and S2 sites are surrounded by four oxygen atoms to form tetrahedra with bond lengths that vary in the ranges of 1.365–1.468 (400 °C) and 1.394–1.497 Å (500 °C) for the S1 site, and 1.393–1.444 (400 °C) and 1.391–1.503 Å (500 °C) for the S2 site. Structural refinement revealed a strong distortion of the $S2O_4$ tetrahedron from 0.002 (25 °C) to 0.018 (400 °C) and 0.039 (500 °C) [47], apparently due to the S2 atom being located in a special site. This confirms data from [34] on some rotation of the tetrahedron, leading to negative thermal expansion. The *M*–O–*T* angles in microblocks vary in the ranges of 141.8(4)–136.3(6)° (Y1–O5–S1) and 161.0(3)–160.9(5)° (Y1–O4–S2) with increasing temperature from 400 to 500 °C. The distance between the activator ion sites is slightly reduced. For example, the closest distances between Y1 sites are reduced from 4.99 to 4.98 Å.

3.6. Photoluminescence Properties

Luminescence spectra obtained with excitation at a wavelength of 375 nm at different temperatures for $(Y_{0.83}Eu_{0.17})_2(SO_4)_3$ phosphor are shown in Figure 9a. In the spectra, all bands correspond to radiative transitions of Eu^{3+} ions. The CIE chromaticity coordinates (x = 0.622, y = 0.377) correspond to the red color (Figure 9b). Obviously, the intensity of the luminescence bands practically does not change up to a temperature of 500 °C. The change in the local environment can be estimated by the asymmetry ratio, which is determined as the integral intensity ratio of radiative transitions $^5D_0$-$^7F_2$ to $^5D_0$-$^7F_1$ for Eu^{3+} ions.

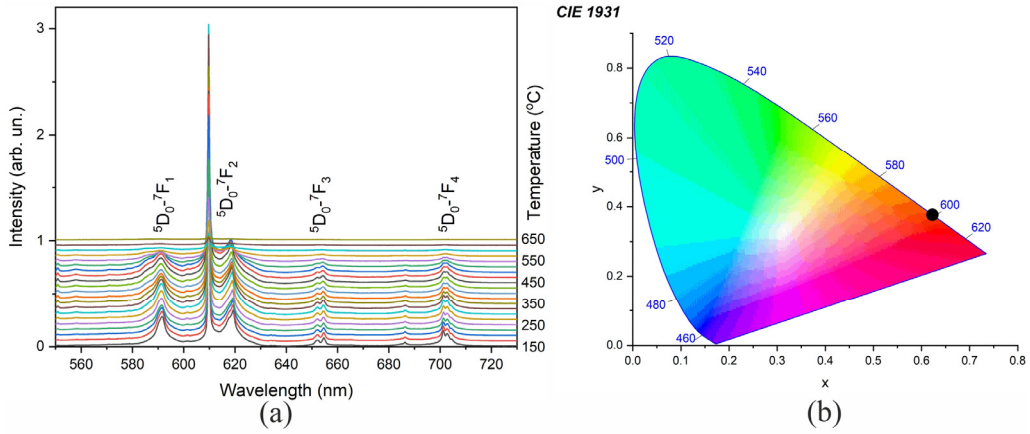


Figure 9. Luminescence spectra for $(Y_{0.83}Eu_{0.17})_2(SO_4)_3$ phosphor at different temperatures during heating upon 375 nm excitation (**a**). Chromaticity diagram (**b**).

3.7. Anti-Thermal Quenching of Luminescence and Crystal Structure

Figure 10 shows the graphs of the dependence of the luminescence quantum yield and the asymmetry coefficient of the europium environment. Red and blue triangles indicate values during heating and cooling, respectively. It is clearly seen that in the temperature range from 150 to 500 °C the symmetry of the europium ions environment does not change, which indirectly indicates the constancy of the phase. At the same time, with an increasing temperature in this range, a monotonic increase in the quantum yield of luminescence is

observed. Such temperature dependence is anomalous and is most likely associated with a negative thermal expansion.

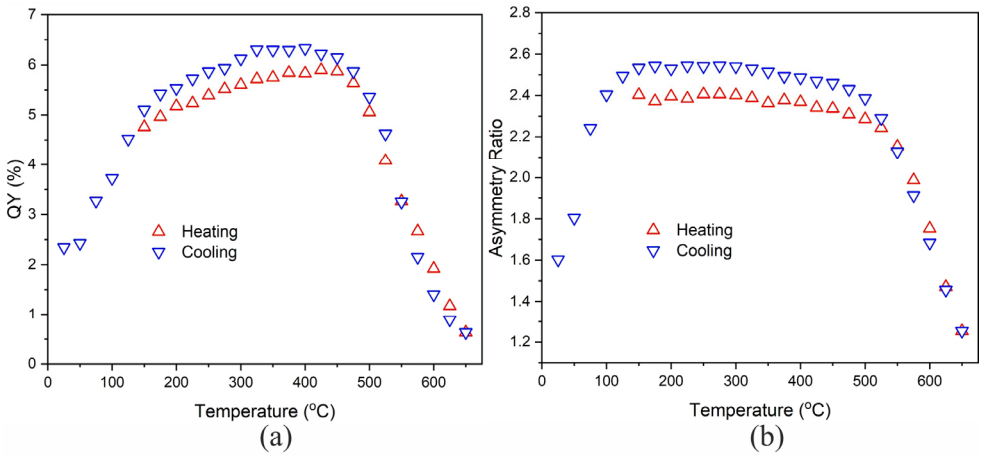


Figure 10. Temperature dependencies of quantum yield (**a**) and asymmetry ratio (**b**) under heating (red triangles) and cooling (blue triangles) conditions for $(Y_{0.83}Eu_{0.17})_2(SO_4)_3$ phosphor.

In many phosphors with anti-thermal quenching of luminescence [6], the two mechanisms of anti-thermal quenching are described. The first mechanism is the presence of positive oxygen vacancies (traps) due to heterovalent isomorphism under doping. As the temperature increases, the electrons are stored at the trapping level and are subsequently transferred to the Eu^{3+} ions, resulting in enhanced red emission. The second mechanism is the reduction of the distance between luminescence centers in the crystal structure due to negative thermal expansion. It is obvious, that in $Y_2(SO_4)_3$:Eu^{3+} phosphors only the second mechanism is realized because of $Y^{3+} \rightarrow Eu^{3+}$ substitution.

The energy transfer between luminescence centers is primarily influenced by the distance between the sites occupied by the activator ions within the crystal structure. According to Dexter's theory [48], an exchange interaction requires a critical distance of 5 Å or less. Typically, as doping concentration increases, the emission intensity tends to decrease, which can be attributed to the dipole-dipole interactions among the Eu^{3+} ions. The probability of these interactions rises as the distance between the active ions decreases. The distances between Y sites in different directions of the crystal structure are 4.95, 5.50, 5.70, 5.73, and 6.50 Å, respectively. Therefore, the energy migration in the $Y_2(SO_4)_3$:Eu^{3+} phosphors is three-dimensional.

The critical energy transfer distance R_c can be calculated using an equation proposed in [22]:

$$R_c \approx 2[3V/4\pi x_c N]_3^1$$

where x_c is the critical doping content, N is the number of sites in the unit cell that can be occupied by activator ions, and V is the volume of the unit cell. For x = 0.17 solid solution at 140 °C, the critical energy transfer distance *Rc* is 5.75 Å. The critical distance is insignificantly decreased with increasing temperature. For example, *Rc* is 5.74 and 5.73 Å for x = 0.17 solid solutions at 400 and 600 °C.

As discussed in Section 3.3, at room temperature, the distance between these sites is 4.95 Å. The Y sites from neighboring chains, which are 5.50, 5.70, and 6.50 Å, conversely, move closer to each other with increasing temperatures. Thus, the probability of dipole-dipole interactions between the nearest sites with a distance of less than 5 Å, which includes Eu^{3+} ions, increases. The distance between the luminescence centers located further than 5 Å decreases, which causes an increase in luminescence with temperature.

4. Conclusions

Novel perspective red-emitting $(Y_{1-x}Eu_x)_2(SO_4)_3$ phosphors (x = 0, 0.17, 0.33, 0.5, 0.66) exhibiting anti-thermal quenching properties due to negative thermal expansion were obtained by crystallization from aqueous solutions. The crystal structure of $Y_2(SO_4)_3$ is characterized as a framework composed of corner-sharing SO_4 tetrahedra and YO_6 octahedra. The crystal structure of the x = 0.5 solid solution was refined at 400 and 500 °C to R_B = 1.70 and 1.94%, respectively. The rotation of the SO_4 tetrahedra contributes to negative volume thermal expansion. The thermal expansion of all samples was analyzed using high-temperature X-ray powder diffraction, revealing that the negative thermal expansion is highly anisotropic ($\alpha_a = -7(3)$, $\alpha_b = -15(3)$, $\alpha_c = -22(2)$, $\alpha_V = -44(2) \cdot 10^{-6}$ °C^{-1} at 500 °C for $YEu(SO_4)_3$). The volumetric thermal expansion of the samples x = 0, 0.17 and 0.50 belongs to a giant negative thermal expansion. The photoluminescence intensity significantly increases (1.8 times) with temperature, reaching up to 500 °C. The anti-thermal quenching of Eu^{3+} luminescence can be attributed to thermally enhanced energy transfer between Eu^{3+} ions, facilitated by the negative thermal expansion of the $(Y_{1-x}Eu_x)_2(SO_4)_3$ solid solutions in all non-equivalent directions. $(Y_{1-x}Eu_x)_2(SO_4)_3$ phosphors can be suitable for developing optical temperature sensors.

Supplementary Materials: The following supporting information can be downloaded at https://www.mdpi.com/article/10.3390/cryst14121074/s1. Table S1: Structure refinement details and crystallographic data for $YEu(SO_4)_3$ at different temperatures; Table S2: Chemical composition of $(Y_{1-x}Eu_x)_2(SO_4)_3$ phosphors (at.%).; Figure S1 The Rietveld refinement of the $YEu(SO_4)_3$ crystal structure using powder X-ray diffraction data at 400 °C. The measured data is represented by a blue line, the refinement fit by a red line and the difference between the data and refinement fit by a gray line; Figure S2; The Rietveld refinement of the $YEu(SO_4)_3$ crystal structure using powder X-ray diffraction data at 500 °C. The measured data is represented by a blue line, the refinement fit by a red line and the difference between the data and refinement fit by a gray line.

Author Contributions: Conceptualization, A.P.S., R.S.B. and S.K.F.; methodology, A.P.S., O.Y.S., A.V.P., S.Y.J., M.G.K. and S.K.F.; software, A.P.S. and O.Y.S.; validation, A.P.S., R.S.B., M.G.K., O.Y.S. and S.K.F.; formal analysis, A.P.S., A.V.P., R.S.B. and S.K.F.; investigation, O.Y.S., A.P.S., A.V.P., M.G.K., R.S.B., S.Y.J. and V.L.U.; resources, S.K.F., R.S.B., M.G.K. and A.V.P.; data curation, R.S.B., M.G.K. and A.V.P.; writing—original draft preparation, A.P.S. and O.Y.S.; writing—review and editing, A.P.S., O.Y.S., A.V.P., R.S.B., M.G.K., S.Y.J. and S.K.F.; visualization, O.Y.S., A.P.S., A.V.P. and R.S.B.; supervision, R.S.B. and S.K.F.; project administration, S.K.F.; funding acquisition, S.K.F. All authors have read and agreed to the published version of the manuscript.

Funding: This work was supported by the Russian Science Foundation [grant number 22-13-00317] (data evaluation and generalization, XRD and photoluminescence experiments and absorption spectroscopy), and the Ministry of Science and Higher Education of the Russian Federation within the scientific tasks of the Institute of Silicate chemistry of Russian Academy of Sciences [project number 1023033000085-7-1.4.3] (synthesis).

Data Availability Statement: CCDC 2401196 and 2401199. contain the crystallographic data for this paper. These data can be obtained free of charge via https://www.ccdc.cam.ac.uk/Community/Depositastructure/CSDCommunications (accessed on 7 November 2024).

Acknowledgments: The X-ray diffraction experiments were performed at The Centre for X-ray Diffraction Studies (Saint-Petersburg State University). The luminescence and absorption spectroscopy were performed at the Center for Optical and Laser Materials Research, Research Park of Saint-Petersburg State University. The chemical analysis was performed at the Centre for Microscopy and Microanalysis of Saint Petersburg State University).

Conflicts of Interest: The authors declare no conflicts of interest.

References

1. Li, L.; Peng, M.; Viana, B.; Wang, J.; Liu, B.; Lei, Y.; Zhang, Q.; Qiu, J. Unusual concentration induced antithermal quenching of the Bi^{2+} emission from $Sr_2P_2O_7$: Bi^{2+}. *Inorg. Chem.* **2015**, *54*, 6028–6034. [CrossRef] [PubMed]
2. Huang, X. Red phosphor converts white LEDs. *Nat. Photonics* **2014**, *8*, 748–749. [CrossRef]

3. Shang, M.; Lin, C.; Li, J. How to produce white light in a single-phase host? *Chem. Soc. Rev.* **2014**, *43*, 1372–1386. [CrossRef] [PubMed]
4. Dai, P.; Zhang, C.; Li, X.; Chen, J.; Xu, X.; Wang, X.; Jia, Y.; Wang, X.; Liu, Y. A single Eu^{2+}-activated high-color-rendering oxychloride white-light phosphor for white-lightemitting diodes. *Light Sci. Appl.* **2016**, *5*, e16024. [CrossRef] [PubMed]
5. Zhou, L.; Wang, W.; Nan, S.; Yu, B.; Zhu, Y.; Shi, Y.; Shi, H.; Zhao, X.; Lu, Z. Single-phase $LiY(MoO_4)_{2-x}(WO_4)_x$:Dy^{3+},Eu^{3+} phosphors with white luminescence for white LEDs. *Mater. Res. Bull.* **2016**, *84*, 429–436. [CrossRef]
6. Zhou, L.; Wang, W.; Xu, D.; Wang, Z.; Yi, Z.; Wang, M.; Lu, Z. Anti-thermal quenching of Eu^{3+} luminescence in negative thermal expansion $Zr(WO_4)_2$. *Ceram. Int.* **2021**, *47*, 34820–34827. [CrossRef]
7. Mondal, K.; Singh, D.K.; Manam, J. Spectroscopic behavior, thermal stability and temperature sensitivity of Ca_2SiO_4: Eu^{3+} red emitting phosphor for solid state lighting application. *J. Alloys Compd.* **2018**, *761*, 41–51. [CrossRef]
8. Zhong, J.; Chen, D.; Peng, Y.; Lu, Y.; Chen, X.; Li, X.; Ji, Z. A review on nanostructured glass ceramics for promising application in optical thermometry. *J. Alloys Comp.* **2018**, *763*, 34–48. [CrossRef]
9. Yadav, R.S.; Rai, S.B. Surface analysis and enhanced photoluminescence via Bi^{3+} doping in a Tb^{3+} doped Y_2O_3 nano-phosphor under UV excitation. *J. Alloys Comp.* **2017**, *700*, 228–237. [CrossRef]
10. Hu, G.; Hu, X.; Chen, W.; Cheng, Y.; Liu, Z.; Zhang, Y.; Liang, X.; Xiang, W. Luminescence properties and thermal stability of red phosphor Mg_2TiO_4: Mn^{4+} additional Zn^{2+} sensitization for warm W-LEDs. *Mater. Res. Bull.* **2017**, *95*, 277–284. [CrossRef]
11. Bondzior, B.; Stefańska, D.; Kubiak, A.; Dereń, P.J. Dipole–dipole and dipole–quadrupole interactions between Sm^{3+} ions in $K_4BaSi_3O_9$. *J. Lumin.* **2017**, *190*, 123–127. [CrossRef]
12. Mikalauskaite, I.; Raudonyte-Svirbutaviciene, E.; Linkeviciute, A.; Urbonas, M.; Katelnikovas, A. Luminescence and luminescence quenching of $Sr_3Lu_2(Si_3O_9)_2$: Ce^{3+} phosphors. *J. Lumin.* **2017**, *184*, 185–190. [CrossRef]
13. Jansen, T.; Jüstel, T.; Kirm, M.; Mägi, H.; Nagirnyi, V.; Tõldsepp, E.; Vielhauer, S.; Khaidukov, N.M.; Makhov, V.N. Site selective, time and temperature dependent spectroscopy of Eu^{3+} doped apatites (Mg, Ca, Sr)$_2Y_8Si_6O_{26}$. *J. Lumin.* **2017**, *186*, 205–211. [CrossRef]
14. Wang, B.; Lin, H.; Huang, F.; Xu, J.; Chen, H.; Lin, Z. Non-rare-earth $BaMgAl_{10-2x}O_{17}$: xMn^{4+}, xMg^{2+}: A narrow-band red phosphor for use as a high-power warm w-LED. *Chem. Mater.* **2016**, *28*, 3515–3524. [CrossRef]
15. Chen, D.; Zhou, Y.; Xu, W.; Zhong, J.; Ji, Z.; Xiang, W. Enhanced luminescence of Mn^{4+}: $Y_3Al_5O_{12}$ red phosphor via impurity doping. *J. Mater. Chem.* **2016**, *4*, 1704–1712. [CrossRef]
16. Melato, L.T.; Motaung, T.E.; Ntwaeaborwa, O.M.; Motloung, S.V. Effect of annealing at different time intervals on the structure, morphology and luminescent properties of $MgAl_2O_4$: 0.3% In^{3+} nanophosphor prepared by citrate sol-gel method. *Opt. Mater.* **2017**, *66*, 319–326. [CrossRef]
17. Zhang, X.; Fu, Z.; Sun, Z.; Liu, G.; Jeong, J.H.; Wu, Z. Temperature-induced phase transition and temperature sensing behavior in Yb^{3+} sensitized Er^{3+} doped YPO_4 phosphors. *Opt. Mater.* **2016**, *60*, 526–532. [CrossRef]
18. Dai, P.; Lee, S.P.; Chan, T.S.; Huang, C.H.; Chiang, Y.W.; Chen, T. $Sr_3Ce(PO_4)_3$: Eu^{2+}: A broadband yellow-emitting phosphor for near ultraviolet-pumped white light-emitting devices. *J. Mater. Chem.* **2016**, *4*, 1170–1177. [CrossRef]
19. Zhang, Y.; Li, Y. Red photoluminescence and crystal structure of $Sr_3Y_2(BO_3)_4$. *Alloys Compd.* **2004**, *384*, 88–92. [CrossRef]
20. Shablinskii, A.P.; Kolesnikov, I.E.; Bubnova, R.S.; Povolotskiy, A.V.; Lähderanta, E.; Filatov, S.K. A novel thermally stable $Ba_3Bi_2(BO_3)_4$:Eu^{3+} red phosphor for solid state lighting application. *J. Lumin.* **2019**, *216*, 116714. [CrossRef]
21. Volkova, E.A.; Maltsev, V.V.; Antipin, A.M.; Deyneko, D.V.; Nikiforov, I.V.; Spassky, D.A.; Marchenko, E.I.; Mitina, D.D.; Kosorukov, V.L.; Yapaskurt, V.O.; et al. The Synthesis, Structure, and Luminescent Properties of $TmMgB_5O_{10}$ Crystals. *Materials* **2023**, *16*, 6084. [CrossRef]
22. Blasse, G. Energy transfer in oxidic phosphors. *Phys. Lett.* **1968**, *28*, 444–445. [CrossRef]
23. Wang, X.; Wang, L.; Takeda, T.; Funahashi, S.; Suehiro, T.; Hirosaki, N.; Xie, R. Blueemitting $Sr_3Si_{8-x}Al_xO_{7+x}N_{8-x}$:$Eu^{2+}$ discovered by a single-particle-diagonosis approach: Crystal structure, luminescence, scale-up synthesis, and its abnormal thermal quenching behavior. *Chem. Mater.* **2015**, *27*, 7689–7697. [CrossRef]
24. Yuan, X.; Zheng, J.; Zeng, R.; Jing, P.; Ji, W.; Zhao, J.; Yang, W.; Li, H. Thermal stability of Mn^{2+} ion luminescence in Mn-doped core-shell quantum dots. *Nanoscale* **2014**, *6*, 300–307. [CrossRef] [PubMed]
25. Long, J.; Chu, F.; Wang, Y.; Zhao, C.; Dong, W.; Yuan, X.; Ma, C.; Wen, Z.; Ma, R.; Du, M.; et al. $M_8MgSc(PO_4)_7$:xDy^{3+} (M = Ca/Sr) single-phase full-color phosphor with high thermal emission stability. *Inorg. Chem.* **2017**, *56*, 10381–10386. [CrossRef]
26. Kang, F.; Peng, M.; Zhang, Q.; Qiu, J. Abnormal anti-quenching and controllable multi-transitions of Bi^{3+} luminescence by temperature in a yellow-emitting $LuVO_4$: Bi^{3+} phosphor for UV-converted white LEDs. *Chem. Eur. J.* **2014**, *20*, 11522–11530. [CrossRef]
27. Zheng, J.; Wu, S.; Chen, G.; Dang, S.; Zhuang, Y.; Guo, Z.; Lu, Y.; Cheng, Q.; Chen, C. Blue-emitting $Ca_5(PO_4)_3Cl$:Eu^{2+} phosphor for near-UV pumped light emitting diodes: Electronic structures, luminescence properties and LED fabrications. *J. Alloys Compd.* **2016**, *663*, 332–339. [CrossRef]
28. Poncé, S.; Jia, Y.; Giantomassi, M.; Mikami, M.; Gonze, X. Understanding thermal quenching of photoluminescence in oxynitride phosphors from first principles. *J. Phys. Chem.* **2016**, *120*, 4040–4047. [CrossRef]
29. Chen, X.; Zhang, Z.; Feng, A.; Xu, M.; Zhao, J.; Xu, F. Electronic structure, optical and thermal/concentration quenching properties of $Lu_{2-2x}Eu_{2x}WO_6$ ($0 \leq x \leq 0.2$). *Mater. Res. Bull.* **2015**, *70*, 26–31. [CrossRef]

30. Zou, H.; Yang, X.; Chen, B.; Du, Y.; Ren, B.; Sun, X.; Qiap, X.; Zhang, Q.; Wang, F. Thermal Enhancement of Upconversion by Negative Lattice Expansion in Orthorhombic $Yb_2W_3O_{12}$. *Angew. Chem.* **2019**, *58*, 17255–17259. [CrossRef] [PubMed]
31. Dang, P.; Li, G.; Yun, X.; Zhang, Q.; Liu, D.; Lian, H.; Shang, M.; Lin, J. Thermally stable and highly efficient red-emitting Eu^{3+}-doped $Cs_3GdGe_3O_9$ phosphors for WLEDs: Non-concentration quenching and negative thermal expansion. *Light Sci. Appl.* **2021**, *10*, 29. [CrossRef] [PubMed]
32. Kim, Y.; Arunkumar, P.; Kim, B.; Unithrattil, S.; Kim, E.; Moon, S.; Hyun, J.; Kim, K.; Lee, D.; Lee, J.; et al. A zero-thermal-quenching phosphor. *Nat. Mater.* **2017**, *16*, 543–550. [CrossRef]
33. Evans, J.S.O.; Mary, T.A.; Sleight, A.W. Negative thermal expansion in a large molybdate and tungstate family. *J. Solid. State Chem.* **1997**, *13*, 580–583. [CrossRef]
34. Evans, J.S.O.; Mary, T.A.; Sleight, A.W. Negative thermal expansion in $Sc_2(WO_4)_3$. *J. Solid. State Chem.* **1998**, *137*, 148–160. [CrossRef]
35. Evans, J.S.O. Negative thermal expansion materials. *J. Chem.* Soc. *Dalton Trans* **1999**, 3317–3326. [CrossRef]
36. Sleight, A.W. Negative thermal expansion materials. *Curr. Opin. Solid State Mater. Sci.* **1998**, *3*, 128–131. [CrossRef]
37. Bubnova, R.S.; Firsova, V.A.; Volkov, S.N.; Filatov, S.K. RietveldToTensor: Program for processing powder X-ray diffraction data under variable conditions. *Glass Phys. Chem.* **2018**, *44*, 33–40. [CrossRef]
38. Shablinskii, A.P.; Povolotskiy, A.V.; Yuriev, A.A.; Biryukov, Y.P.; Bubnova, R.S.; Avdontceva, M.S.; Janson, S.Y.; Filatov, S.K. Novel Red-Emitting $BaBi_2B_4O_{10}$:Eu^{3+} Phosphors: Synthesis, Crystal Structure and Luminescence. *Symmetry* **2023**, *15*, 918. [CrossRef]
39. Evans, J.S.O.; Mary, T.A.; Sleight, A.W. Structure of $Zr_2(WO_4)(PO_4)_2$ from Powder X-Ray Data: Cation Ordering with No Superstructure. *J. Solid State Chem.* **1995**, *120*, 101–104. [CrossRef]
40. Held, P.; Wickleder, M. Yttrium(III) sulfate octahydrate. *Acta Cryst.* **2003**, *59*, 98–100. [CrossRef]
41. Wickleder, M.S. Wasserfreie Sulfate der Selten-Erd-Elemente: Synthese und Kristallstruktur von $Y_2(SO_4)_3$ und $Sc_2(SO_4)_3$. *Z. Fuer Anorg. Allg. Chem.* **2000**, *626*, 1468–1472. [CrossRef]
42. Hartenbach, I.; Schleid, T. Serendipitous formation of single-crystalline $Eu_2O_2(SO_4)$. *Z. Fuer Anorg. Allg. Chem.* **2002**, *628*, 2171. [CrossRef]
43. Grima, J.N.; Zammit, V.; Gatt, R. Negative thermal expansion. *Xjenza* **2006**, *11*, 17–29.
44. Takenaka, K. Progress of Research in Negative Thermal Expansion Materials: Paradigm Shift in the Control of Thermal Expansion. *Front. Chem.* **2018**, *6*, 267. [CrossRef]
45. Liang, E.; Sun, Q.; Yuan, H.; Wang, G.; Zeng, G.; Gao, Q. Negative thermal expansion: Mechanisms and materials. *Front. Phys.* **2021**, *16*, 53302. [CrossRef]
46. Voronkov, A.A.; Ilyukhin, V.V.; Belov, N.V. Crystal chemistry of mixed frameworks. Principles of Their Formation. *Kristallogr* **1975**, *20*, 556–566. (In Russian)
47. Baur, W.H. The geometry of polyhedral distortions. Predictive relationships for the phosphate group. *Acta Crystallogr. B* **1974**, *30*, 1195–1215. [CrossRef]
48. Dexter, D.L. A theory of sensitized luminescence in solids. *J. Chem. Phys.* **1953**, *21*, 836–850. [CrossRef]

Disclaimer/Publisher's Note: The statements, opinions and data contained in all publications are solely those of the individual author(s) and contributor(s) and not of MDPI and/or the editor(s). MDPI and/or the editor(s) disclaim responsibility for any injury to people or property resulting from any ideas, methods, instructions or products referred to in the content.